Editors' Suggestion

Order and disorder in the magnetization of the chiral crystal $CrNb_3S_6$

Gary W. Paterson,[1,*] Tsukasa Koyama,[2] Misako Shinozaki,[3] Yusuke Masaki,[4] Francisco J. T. Goncalves,[5,†] Yusuke Shimamoto,[5] Tadayuki Sogo,[5] Magnus Nord,[1] Yusuke Kousaka,[6,‡] Yusuke Kato,[3] Stephen McVitie,[1] and Yoshihiko Togawa[5,†]

[1]*SUPA, School of Physics and Astronomy, University of Glasgow, Glasgow G12 8QQ, United Kingdom*
[2]*Department of Materials Science, Osaka Prefecture University, Sakai, Osaka 599-8531, Japan*
[3]*Department of Basic Science, The University of Tokyo, Meguro, Tokyo 153-8902, Japan*
[4]*Department of Physics, The University of Tokyo, Bunkyo-ku, Tokyo 113-0033, Japan*
[5]*Department of Physics and Electronics, Osaka Prefecture University, 1-1 Gakuencho, Sakai, Osaka 599-8531, Japan*
[6]*Research Institute for Interdisciplinary Science, Okayama University, Okayama, Okayama 700-8530, Japan*

(Received 2 April 2019; published 26 June 2019)

Competing magnetic anisotropies in chiral crystals with Dzyaloshinskii-Moriya exchange interactions can give rise to nontrivial chiral topological magnetization configurations with new and interesting properties. One such configuration is the magnetic soliton, where the moment continuously rotates about an axis. This magnetic system can be considered to be one dimensional and, because of this, it supports a macroscale coherent magnetization, giving rise to a tunable chiral soliton lattice (CSL) that is of potential use in a number of applications in nanomagnetism and spintronics. In this paper, we characterize the transitions between the forced-ferromagnetic (F-FM) phase and the CSL one in $CrNb_3S_6$ using differential phase contrast imaging in a scanning transmission electron microscope, conventional Fresnel imaging, ferromagnetic resonance spectroscopy, and mean-field modeling. We find that the formation and movement of dislocations mediate the formation of CSL and F-FM regions and that these strongly influence the highly hysteretic static and dynamic properties of the system. Sample size and morphology can be used to tailor the properties of the system and, with the application of magnetic field, to locate and stabilize normally unstable dislocations and modify their dimensions and magnetic configurations in ways beyond that predicted to occur in uniform films.

DOI: 10.1103/PhysRevB.99.224429

I. INTRODUCTION

Since the general theory of helicoidal magnetic structures was proposed [1] and experimentally confirmed in $CrNb_3S_6$ [2], there has been much interest in this [3,4] and other [5] chiral systems for the many unusual properties they possess. The helimagnetism in $CrNb_3S_6$ originates from its monoaxial chiral hexagonal crystal belonging to the $P6_322$ space group [6], which supports a large uniaxial anisotropy K_u along the chiral c axis, symmetric Heisenberg exchange interactions, and antisymmetric Dzyaloshinskii-Moriya exchange interactions (DMIs), D [7,8]. The magnetization in zero applied field ($H = 0$) is in a chiral helimagnetic (CHM) phase, where the moment continuously rotates in the ab plane, along the c axis. The intrinsic soliton periodicity in zero applied field $L(H = 0)$ depends on the ratio of the energy parallel to the c axis, $J_\parallel$, to the DMI energy, and is 48 nm [6,9].

When a magnetic field is applied perpendicular to the c axis, a net moment arises as the spins preferentially align with the magnetic field and the incommensurate CHM phase continuously transforms into the chiral soliton lattice (CSL) phase. At sufficiently high fields, this creates regions of forced-ferromagnetic (F-FM) order, indicated by the yellow arrows in the schematic in Fig. 1, between which are isolated solitons where the moments rotate through 2π, as depicted by the orange to green colored arrows. As the field is increased, the F-FM regions grow in extent through distortion and then expulsion of solitons from the system until at some critical field H_c the entire system is in the F-FM phase. Theoretical [11] and experimental [12] phase diagrams for $CrNb_3S_6$ have been constructed. The critical paramagnetic temperature depends on the crystal quality but is typically ∼127 K, while the critical field for the CSL to F-FM transition varies due to sample thickness-related demagnetization effects, but is typically around 2 kOe [6,9].

Importantly, because the transition between the CSL and F-FM phases is continuous, the point at which the region between the magnetic kinks may be regarded as a F-FM *domain* and not as part of a dilute CSL is not well defined, and will likely depend on the property of interest, e.g., static or dynamic properties. In this paper, we take the phenomenological approach and refer to *regions* of CSL or F-FM, depending on their most prominent character.

$CrNb_3S_6$ is unique among the helicoidal materials in that the magnetic ordering phase coherence extends over macroscopic dimensions [2]. It is this protected property of the

*Gary.Paterson@glasgow.ac.uk
†Also at Chirality Research Center (CResCent), Hiroshima University, Higashi-Hiroshima, Hiroshima 739-8526, Japan.
‡Also at Center for Chiral Science, Hiroshima University, Higashi-Hiroshima, Hiroshima 739-8526, Japan; present address: Department of Physics and Electronics, Osaka Prefecture University, 1-1 Gakuencho, Sakai, Osaka 599-8531, Japan.

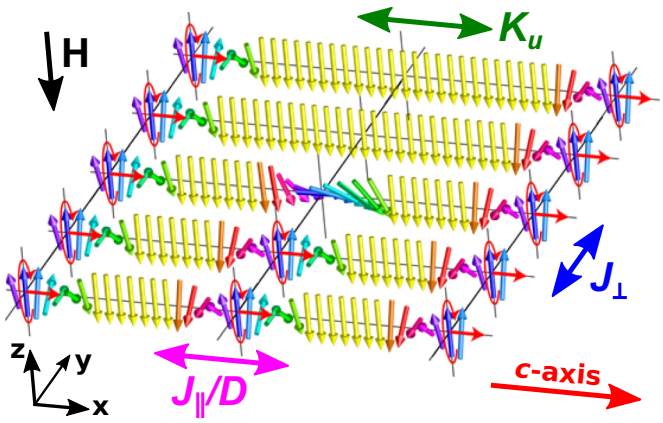

FIG. 1. Schematic representation of a chiral soliton lattice (CSL) with a dislocation created by a magnetic field H applied downwards. $J_\perp$ (∼140 K), $J_\parallel$ (∼18 K), K_u (∼1 K), and D (∼2.9 K) are the exchange energy densities perpendicular and parallel to the c axis (indicated by the red arrows), and the uniaxial anisotropy and DMI energy density, respectively [10].

magnetic solitons, together with the ease with which the magnetic texture can be modified by the application of field, and the interesting emergent phenomena [3,4] that make $CrNb_3S_6$ potentially useful in many device applications in nanomagnetism and spintronics. Of particular interest are discretization effects arising from changes in the magnetic topology created by the addition or removal of a soliton. These effects have been observed in a variety measurement techniques, including transmission electron microscopy, magnetoresistance, magnetic torque, ferromagnetic resonance, and x-ray circular dichroism [12–15].

Between the CSL and F-FM regimes, dislocations in the soliton lattice such as that depicted by the schematic in Fig. 1 can form and are likely to play a key role in mediating the changes in the magnetic phase of the material. Indeed, recently reported modeling predicts that soliton annihilation occurs through dislocations forming and moving perpendicular to the c axis, while creation occurs in a coherent process at the sample edges [15]. The coherence of the CSL is of great importance to the functionality of the material and it is thus crucial to characterize it.

In this paper, we experimentally characterize the transition from the F-FM phase to the CSL one and back in $CrNb_3S_6$ using Lorentz microscopy and ferromagnetic resonance (FMR) spectroscopy, with a particular focus on magnetic lattice dislocations. We show that dislocations mediate the CSL to F-FM transition. In the opposite transition, dislocations appear as a result of the partitioning of the magnetization into a mixture of CSL and field-polarized F-FM regions, creating a disordered phase. The formation of this disordered phase depends on the reversal direction and creates an asymmetry in the associated dynamic properties. The dislocations are generally metastable or unstable, but we show how they can be localized by "pinning" them against stepped increases in sample thickness, which also allows their dimensions to be modified far beyond that predicted from modeling of uniform thickness samples using a mean-field approach. This observation opens the possibility to localize dislocations and make use of the nanochannels of field-polarized spins created by them in device applications.

After summarizing the methodology or our approach in Sec. II, the mean-field simulations are presented in Sec. III, before the main experimental results are discussed in Sec. IV.

II. METHODOLOGY

A. STEM sample preparation and measurements

To experimentally quantify the magnetic texture in $CrNb_3S_6$, differential phase contrast (DPC) and electron energy loss spectroscopy (EELS) measurements were performed on a cross section of a single-crystal $CrNb_3S_6$ sample in a probe corrected JEOL ARM 200F scanning transmission electron microscope (STEM) equipped with a cold field emission electron gun operated at 200 keV. In the DPC measurements, the sample was cooled to ∼102 K in a Gatan HC3500 sample holder while the signal was collected by a custom eight-segment detector [16], allowing the modified DPC method to be used to reduce diffraction artifacts [17]. During the measurements, the field was applied in a direction perpendicular to the sample and varied by exciting the objective lens to different strengths. The convergence semiangle was 1.31 mrad, giving a spot size of 2.34 nm and a resolution of 1.17 nm; the pixel size was 1.24 nm for the low-field data and 0.74 nm for the high-field data.

The sample thickness was determined from a t/λ map [18] obtained from EELS measurements performed in the same microscope with the objective lens switched on, and an effective Z number of 25.8, calculated using Gatan DIGITAL MICROGRAPH. The EELS spectra were collected using a GIF Gatan Quantum ER spectrometer in the scanning TEM (STEM) mode. The convergence and collection semiangles were 29 and 36 mrad, respectively.

The cross section was prepared in an FEI Nova NanoLab DualBeam focused ion beam (FIB), and thinned to electron transparency using standard lamella preparation procedures. All data were processed using PYTHON and the FPD [19] and HYPERSPY [20] packages.

B. TEM measurements

In order to see the CSL behavior with dislocations qualitatively, Fresnel images were recorded in an underfocus condition (typically ∼1 μm defocus) using a model JEM-2010 or JEM-2100 transmission electron microscope (TEM) operated with an acceleration voltage of 200 kV. The TEM samples were cooled using a liquid N_2 holder for the experiments performed in a temperature range above 100 K. To see the behavior at lower temperatures for many hours, the seventh generation cryogenic transmission electron microscope, available in Nagoya University, Japan [21] was adopted. The samples were cooled to below 2 K using superfluid He and the CSL behavior was examined at low temperatures in magnetic fields systematically.

C. FMR measurements

The magnetization dynamics were studied via FMR experiments using a custom low-temperature system [14]

comprising a vector network analyzer (VNA) coupled to a broadband coplaner waveguide and operated at 50 K. The transmitted power (S_{21}) through the ground-signal-ground waveguide to which the sample was attached (see Fig. S8 [22]) was recorded as a function of frequency as the applied field was reduced from a large positive value ($|H| > H_c$) to a similarly large negative value.

The attenuation of the transmitted signal is strongly frequency dependent and so we normalize the data at each frequency to a high percentile value of the field-dependent data across all fields. This procedure avoids resonances in a reference spectra appearing in the normalized data. The data are further filtered by applying a median line correction to correct small variations in a scattering parameter at different frequencies due to small drifts in the VNA electronics.

D. Simulations

Mean-field simulations were performed for a three-dimensional lattice with the spin Hamiltonian $\mathcal{H}$ given in (1), which consists of ferromagnetic exchange interactions ($J_\parallel$ for bonds parallel to the x axis, $J_\perp$ for bonds perpendicular to the x axis), DM interaction for bonds parallel to the x axis (coupling constant D), easy-plane anisotropy (coupling constant K_u) and Zeeman energy due to the main external field applied along the z axis (H_z), and an infinitesimal field parallel to x axis (H_x) to break the symmetry [10],

$$\begin{aligned}\mathcal{H} = &-J_x \sum_i \boldsymbol{S_i}\cdot(\boldsymbol{S}_{i+\hat{y}} + \boldsymbol{S}_{i+\hat{z}}) - J_{yz}\sum_i \boldsymbol{S_i}\cdot\boldsymbol{S}_{i+\hat{x}} \\ &- D\sum_i (\boldsymbol{S_i}\times\boldsymbol{S}_{i+\hat{x}})\cdot\hat{\boldsymbol{x}} + K_u\sum_i \left(S_i^x\right)^2 \\ &- H_z\sum_i \boldsymbol{S_i}\cdot\hat{\boldsymbol{z}} - H_x\sum_i \boldsymbol{S_i}\cdot\hat{\boldsymbol{x}}. \end{aligned} \tag{1}$$

In the mean-field approximation, local spin $\boldsymbol{S}_i$ (with modulus S) on the site $\boldsymbol{i} = (i_x, i_y, i_z) \in [1, N_x] \otimes [1, N_y] \otimes [1, N_z]$ is subject to the mean field (molecular field) $\boldsymbol{H}_i^{\text{eff}}$ and the expectation value $\langle \boldsymbol{S}_i\rangle$ is given by $\langle \boldsymbol{S}_i\rangle = Sf(S|\boldsymbol{H}_i^{\text{eff}}|/(k_BT))\boldsymbol{H}_i^{\text{eff}}/|\boldsymbol{H}_i^{\text{eff}}|$ with $f(x) = \coth(x - 1/x)$. $\boldsymbol{H}_i^{\text{eff}}$ is given as a function of $\{\langle \boldsymbol{S}_j\rangle\}_j$ and thus the mean-field theory yields a self-consistent equation for $\{\langle \boldsymbol{S}_j\rangle\}_j$.

The iteration procedure to seek for a solution to this self-consistent equation consists of the following steps: (i) Prepare an initial state $\{\langle \boldsymbol{S}_j\rangle\}_j$; (ii) calculate $\boldsymbol{H}_i^{\text{eff}}$ for a given $\{\langle \boldsymbol{S}_j\rangle\}_j$; (iii) update $\langle \boldsymbol{S}_i\rangle$ by $Sf(S|\boldsymbol{H}_i^{\text{eff}}|/(k_BT))\boldsymbol{H}_i^{\text{eff}}/|\boldsymbol{H}_i^{\text{eff}}|$; (iv) repeat (ii) and (iii) until $\{\langle \boldsymbol{S}_j\rangle\}_j$ converges. The updated series of $\langle \boldsymbol{S}_i\rangle$ can be regarded as a kind of relaxation process.

For the present purpose, we focus on a transient time domain, when the dislocations exhibit slow dynamics to annihilation. We take as an initial state with $\boldsymbol{S}_i = S(\cos(2\pi w i_z/N_z), \sin(2\pi w i_z/N_z), 0)$ for $i_y \in [1, N_m]$ and $\boldsymbol{S}_i = S(\cos[2\pi(w+1)i_z/N_z], \sin[2\pi(w+1)i_z/N_z], 0)$ for $i_y \in [N_m + 1, N_y]$ with an integer $N_m \in (1, N_y)$. We take $(N_x, N_y, N_z) = (200, 200, 5)$. The integer w denotes a winding number. Typically, it takes 10000 iterations to relax a state with a pair of dislocation and 80000 iterations to annihilate the pair.

When presented with the projected components of the magnetization, the spacing between spins was taken as 0.575 nm in x, and 1.21 nm in y [9].

III. SIMULATION RESULTS

A. Numerical simulation of chiral soliton lattice dislocations

We begin by describing the expected behavior of edge dislocations formed in the chiral soliton lattice of a uniformly thick sample of $CrNb_3S_6$. Here, we use the term "edge" to describe the dislocation in its crystallographic sense, not in the sample geometry one. To do this, simulations were performed using a self-consistent mean-field approach to solving the spin Hamiltonian [10] with the magnetization formed from a three-dimensional lattice of spins initialized with two dislocations. A periodic system was defined with the c axis along the x axis, with 200 spins in x and y, and 5 in z (see Fig. 1 for orientation definitions). The magnetization parameters used were $D/J_\parallel = 0.16$, $J_\perp/J_\parallel = 8$, $H_z/(J_\parallel S) = 0.01$, $H_\parallel/(J_\parallel S) = 10^{-14}$, and $T/(J_\parallel S^2) = 1$, where S and T are the spin modulus and the temperature, respectively, and $J_\parallel$ and $J_\perp$ are the exchange energy densities along the x axis (parallel to the c axis) and perpendicular to it, respectively.

The magnetization distribution does not converge upon iteration of the calculations, indicating the dislocations are unstable and, instead, the dislocations approach one another and eventually annihilate. In doing so, the spins forming the soliton "untwist" to lie parallel to one another in the direction of the field, creating a region of more dilute CSL. The projected magnetization components part way through this process are depicted in the left-hand column of Fig. 2 and are characteristic of the general distribution. Oscillations in intensity along the x axis in Figs. 2(a) and 2(b) represent rotation of the moment in the ab plane along the c axis, with 2π rotations of the moment between successive peaks or troughs. At the positions of the dislocations, the moment is predicted to rotate in plane to point along the c axis, creating a nonzero x component of magnetization as shown in Fig. 2(c), similar to that depicted in Fig. 1.

To enable comparisons with differential phase contrast (DPC) measurements (discussed later), we display in the middle column of Fig. 2 the calculated integrated induction field components in the plane of the sample that would be imaged in the experiment, using the Fourier space approach to solving the Aharonov-Bohm equation [23]. With the electron beam traveling along a path perpendicular to the film, DPC is insensitive to the z component of the magnetization. The projected in-plane magnetization and induction will differ if the magnetization has any divergence [24]. This is true for the dislocations, so it is important to understand the differences between the magnetization from the model and the measured induction field from Lorentz microscopy. The magnetization divergence is plotted in Fig. S1, and is accompanied by a detailed discussion [22].

The right-hand column of Fig. 2 [Figs. 2(f)–2(h)] shows profiles along the lines in the surface plots [Figs. 2(a), 2(b) and 2(d)] along with fits to the data [thin black lines in Figs. 2(g) and 2(h)] to estimate the feature widths. The y component of the magnetization [Fig. 2(b)] shows the antiparallel

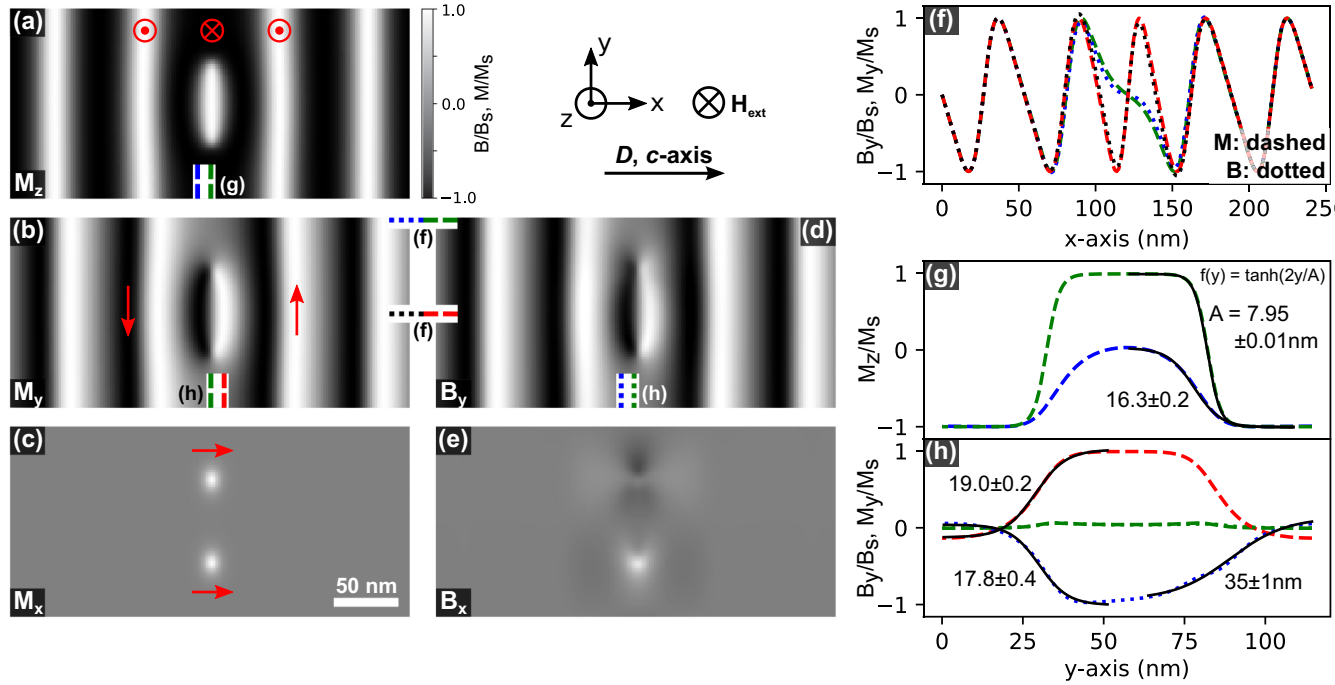

FIG. 2. CSL dislocation simulations with the field applied perpendicular to the c axis. The left-hand column [(a)–(c)] shows the projected magnetization components in an untilted sample. The red arrows indicate the magnetization direction. The middle column [(d) and (e)] shows the calculated integrated magnetic induction components that would be imaged by DPC measurements. The right-hand column [(f)–(h)] shows the profiles at the locations indicated by the colored lines in the surface plots. Dashed lines are M, dotted lines are B. The annotated dimensions are widths A of hyperbolic tangent functions $\tanh(2y/A)$ (black lines) fitted to the data. All data are presented in normalized units and with a common color map.

configuration of the CSL and this is well mapped by the induction field [Fig. 2(d)] at most locations, as indicated by the overlapping data in Figs. 2(f), with subtle differences in the vicinity of the dislocations where there is some divergence of the magnetization. However, the x component of the magnetization [Fig. 2(c)] results from the presence of the dislocation and is divergent in nature. Divergence of magnetization results here from both the x and y components and results in magnetic field sources (H) which will make the projected magnetization and induction components differ. In this case, the nondivergent magnetization dominates the contrast in Fig. 2(d) which is only slightly different from Fig. 2(b), while in Fig. 2(c) the magnetization is mostly divergent and so, not unexpectedly, the contrast in Fig. 2(e) is quite different from in Fig. 2(c). It can be seen that the contrast in Fig. 2(e) is significantly reduced compared to Fig. 2(c) and that opposite ends of the dislocation have a distinctly different character. These differences are shown in more detail in the difference and histogram plots in Figs. S2 and S3 [22], respectively.

For the magnetic configuration depicted in Fig. 2, the moment continually rotates between solitons [see the green and blue lines in Fig. 2(f)], showing that the system may be regarded as a dilute CSL. However, in both the F-FM *and* CSL phases, the spins in the *ab* plane (the yz plane of Figure 1) are parallel to all other spins within the same plane. A dislocation in a CSL marks the location where the spins in the *ab* plane rotate between regions of different spin orientations, as shown in Fig. 2, and thus they may be considered as a kind of domain wall. As in normal ferromagnets, the domain wall width here is predicted to be independent of the applied field strength, and to be proportional to $\sqrt{J_\perp/K_{\text{eff}}}$, where $J_\perp$ is the exchange energy density in the yz plane, perpendicular to the c axis, and K_{eff} is the effective anisotropy which is determined by $J_\parallel$, and the DM interaction (D) and uniaxial anisotropy (K_u) strengths, $K_{\text{eff}} = 2(\sqrt{J_\parallel^2 + D^2} - J_\parallel) + K_u$ [25].

The wall width in this system is most naturally defined as the distance over which the z component of the magnetization reverses. To extract this width, we fit hyperbolic tangent functions to the data, as shown in Fig. 2(g), and find that the best fitting parameters for the profiles are 7.95 nm down the center of the soliton dislocation and 19.0 nm on either side of this. Experimentally, we do not measure this component with DPC imaging, however, it gives useful length scales. Therefore, to be able to compare with experiment, the y component of the integrated induction at its position of maximum (or minimum) strength, displaced laterally from the soliton center, is used as a measure of the dislocation width. By comparison of Figs. 2(a) and 2(b), it is clear that this width will be much wider than the distance over which the z component of the dislocation magnetization M_z reverses. Line profiles of the y components of the magnetization and induction field at the positions indicated by the dotted and dashed lines, respectively, in the images in Figs. 2(b) and 2(d) are plotted in Fig. 2(h) and show that a width parameter of either 17.8 or 35 nm is obtained from the induction variation. At one end of the dislocation, the effect of the H field due to the magnetization divergence is low and the induction and magnetization profiles are very similar, with a width profile of 17.8 nm. However, at the other end there is a much larger

difference due to the increased H field created from the magnetization divergence and the width is larger at 35 nm (see Supplemental Material [22] for a detailed discussion). In terms of the measured numbers, we see that the smaller number of 17.8 nm is comparable to the y and z components of the magnetization off center of the dislocation.

IV. EXPERIMENTAL RESULTS AND DISCUSSION

A. Direct observations of dislocations

To directly observe edge dislocations formed in the chiral soliton lattice of $CrNb_3S_6$, the magnetization state of a thin ($\leqslant$80-nm-thick) lamella sample was investigated using DPC imaging in a scanning transmission electron microscope. Unlike Fresnel imaging (discussed later), DPC is an in-focus Lorentz imaging technique [26] and, with a known sample thickness, allows us to quantitatively measure with high spatial resolution the sample magnetic induction, from which the magnetization state can be inferred. The dislocations, marked in Fig. 3 by a rotated red "$\perp$" symbol, are shown with a low (left column) and high (right column) field applied perpendicular to the c axis. The measured x components of induction (along the c axis) are shown in Fig. S4 [22], and will be discussed later. Unlike in the simulations, in the experiment, these dislocations are metastable at low fields and can be made stable at high fields by sample thickness modulation.

In the low-field case, the stability of the dislocation may not be captured in the simulation due to the finite size of the sample and periodic boundary conditions being imposed, which limits the extent to which the soliton lattice can distort. Instead, the simulation may be more representative of a dilute CSL phase. In the real system, the soliton lattice is dense at low applied field values and gradual lattice deformation occurs around the dislocation, as may be seen in Fig. 3(a). In this case, the equivalence of dislocations and domain walls is somewhat modified; instead of defining a wall between regions of CSL and F-FM, the dislocation may be thought of as defining regions of different soliton kink densities. The large lateral size of the experimental sample means that there are very many solitons and the addition or removal of one soliton can be accommodated more easily through a gradual deformation of the lattice.

Induction profiles parallel to the c axis at the positions of the arrows in Fig. 3(a) are plotted in Fig. 3(b), and the period of the top and bottom series estimated by fitting sinusoidal functions to the data. We use sinusoidal functions since the field used here (104 Oe) is over an order of magnitude smaller than the typical critical field, so the magnetization closely resembles that of the helimagnetic phase expected from the sine-Gordon model [27], the projection of the moment of which is sinusoidal [2]. The CSL periodicity increases from 40 nm below the dislocation to 52 nm above it, straddling the expected low-temperature CHM value of 48 nm, and reflects local distortion of the lattice in the vicinity of the dislocation, as discussed above. From the curvature of the solitons in Fig. 3(a), clearly the lattice deformation is strongest near the dislocation and it extends over multiple soliton periods in all directions.

To map spatially the lattice distortion parallel to the c axis, we Fourier filtered the data in Fig. 3(a) and then fitted sinusoidal functions to overlapping regions across the entire scan. The results of this are shown in Figs. 4(a) and 4(b), where the color map in the period data in Fig. 4(b) is centered around 45.6 nm (gray), with blue indicating shorter periods, and red longer ones. The magnetic lattice is most strongly modified at the location of the dislocation, as one would expect, but distortion of the lattice extends for tens to hundreds of nanometers, demonstrating the significant disturbance to the surrounding lattice created by a single dislocation.

The period profiles from the average of the regions marked by the dashed lines in Fig. 4(b) are shown in Figs. 4(c) and 4(d) for the directions perpendicular (magenta) and parallel (green) to the c axis, respectively. The full width at half maximum value of the distortion parallel to the c axis is around 160 nm. To estimate the distortion length scale in the perpendicular direction, we fitted a decaying exponential function (black line) to the data (magenta) in Fig. 4(c) and extracted a decay constant of around 114 nm.

The mean period value used in the above analysis was extracted from the average period profile perpendicular to the c axis shown in Fig. 4(c) by fitting the function $a/(y - y_o) + p_o$ to the data, where a and y_o are constants and p_o is the predicted period far from the dislocation. Such $1/y$ expressions arise in models of stress in two-dimensional (2D) crystals with edge dislocations [28], but we use it in our one-dimensional (1D) magnetic lattice only to estimate the value of p_o in the measurement. This mean value is also indicated by the dashed black vertical line in Fig. 4(c). In the fit, we excluded the area within 30 nm of the dislocation to avoid inaccuracies arising from using the average profile.

The measured induction profile perpendicular to the c axis, along the center of the dislocation, is shown in Fig. 3(c). The dislocation is approximately 60 nm wide and is much narrower than the long-range lattice distortion, reflecting the relatively weak DMI strength compared to that of the uniaxial anisotropy. This can be understood by considering that the magnetization rotation rate reduces in the immediate vicinity of the dislocation, increasing the DMI contribution to the energy, yet the moment remains very closely aligned with the ab plane throughout because of the larger uniaxial anisotropy contribution to the energy of moments pointing away from the easy axis.

Equivalent induction plots for the high-field case in which the CSL is diluted by wide regions of slowly rotating moments are shown in the right-hand column of Fig. 3. At high fields, dislocations are generally unstable in uniform thickness films, consistent with the simulations, but can, as done here, be stabilized by pinning them up against an energy barrier created by an increasing sample thickness. In the sample images presented here, the thickness begins to increase to several hundred nanometers from just below the bottom edge of the image in Fig. 3(d) (see Fig. S5 for further details [22]).

The soliton profile parallel to the c axis (black line) and the net moment twist rate (blue line) produced from the average of the data outlined with a green dashed line in Fig. 3(d) are shown in Fig. 3(e). Here, the blue, green, and red arrows indicate equivalent points to those similarly marked in Fig. 3(d) and the locations of profiles drawn in the same-colored lines in Fig. 3(f) (discussed later). Since the magnetization at locations far from dislocations is free of divergence, the saturation

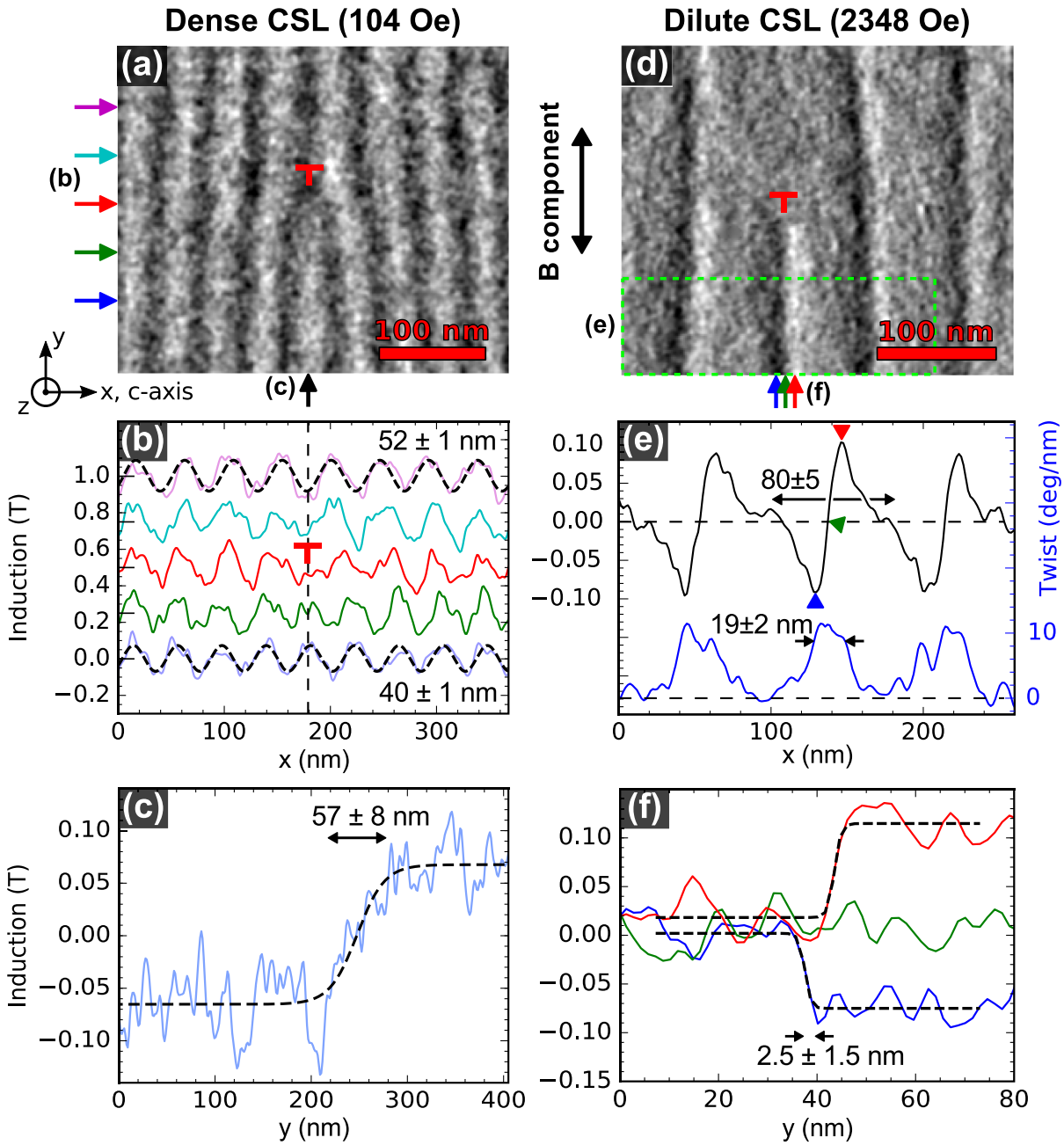

FIG. 3. Induction maps of dislocations at low (left column, 104 Oe) and high (right column, 2348 Oe) fields, measured using DPC imaging at a temperature of 102 K. (a) and (d) show the component of the induction perpendicular to the field applied into the page, where the dislocations are marked by a rotated red "⊥" symbol. (b) Line profiles along the *c* axis at positions indicated by the arrows in (a). (c) Induction profile along the center of the low-field dislocation, marked by the vertical arrow in (b). Soliton profiles parallel and perpendicular to the *c* axis at high field are shown in (e) and (f), respectively. The colored arrows in (d) and (e) indicate common locations, and are those of the matching colored lines in (f). The data in (e) were produced from average of the region outlined with a green dashed line in (d). The dashed lines in (b), (c), and (f) are fits to the data of sinusoidal and hyperbolic tangent functions. The lower (blue) line in (e) is the rotation rate of the high-field solitons. The dimension in (e) is the average over the three leftmost solitons shown in (d), while that in (f) is the average of the two profiles along the maxima (red) and minima (blue) of the high-field dislocation. The errors quoted are from the fits to the data with an additional error estimated from a calibration measurement, except in (e), where the value and error are the mean and standard deviation of the measurements of the three solitons shown.

magnetization can be inferred directly from the integrated induction from the DPC measurement and is $\mu_o M_s \approx$ 0.07–0.1 T. This is similar to values reported from selected area electron diffraction measurements of lamella at 110 K of 0.086 T, corresponding to $1.5\mu_b$/Cr [2], and of $1.9\mu_b$/Cr [9] in bulk samples at a temperature of 102 K. The average trough to peak (blue to red arrow) distance is ∼19 nm, and is considerably narrower than half the ∼80 nm full width of the soliton, shown in Fig. 3(e), demonstrating how the soliton structure is modified at high fields to reduce the Zeeman energy. This can

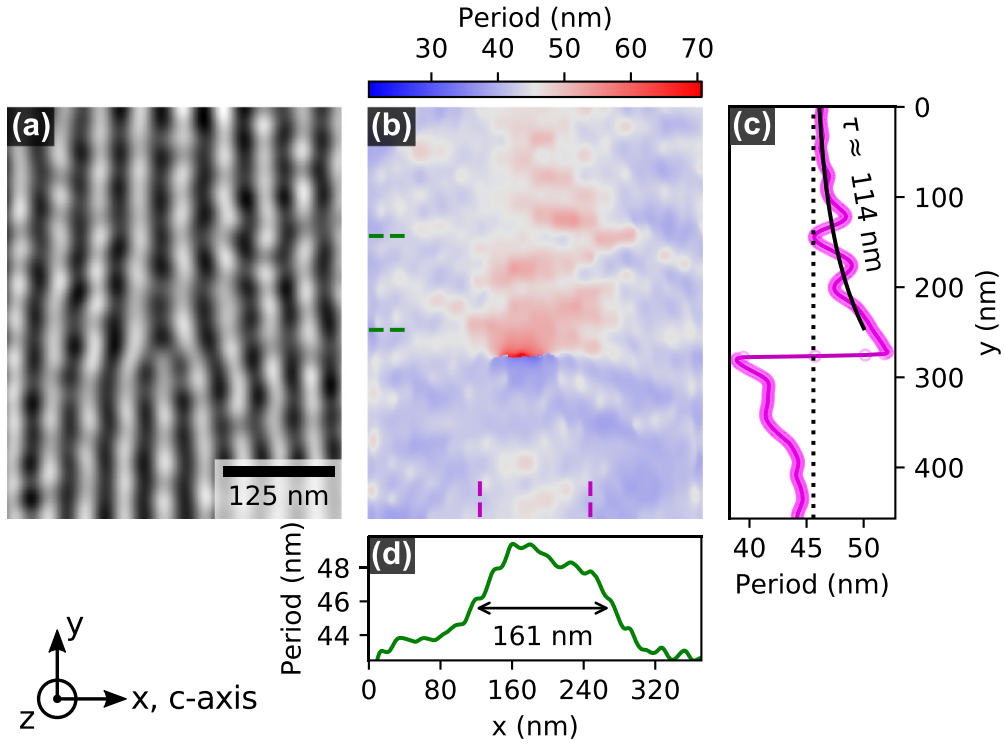

FIG. 4. CSL deformation around the low-field dislocation in the DPC data in Fig. 3(a). (a) Fourier filtered data. (b) Local CSL periodicity obtained by fitting a sinusoidal function to overlapping 88 nm sections along each row of the filtered data. Note that the fitting width limits the accuracy in close proximity to the dislocation, but otherwise accurately measures the magnitude and extent of the lattice distortion. (c) and (d) show periodicity profiles from the average of the areas delimited by the similarly colored dashed lines in (b). The black line in (c) is an exponential fit to the decay in period perpendicular to the c axis, while the dimension in (d) is the approximate full width at half maximum value of the distortion parallel to the c axis.

be seen in Fig. 3(e) by the asymmetry of the induction gradient on each side of the maxima or minima, matching that in the simulation [cf. Fig. 2(f)], and appears as a narrower rotation between troughs and peaks in the twist rate data when moving from left to right along the graphs (between the blue and red arrows). The maximum rate is $\sim 11^\circ$/nm, which would give a period of only ~33 nm if the rate is maintained across the soliton. The region of faster rotation will correspond to that in the sample where a component of the moment points antiparallel to the applied field which, in this case, points into the page.

The three colored lines in Fig. 3(f) show the induction profile across the dislocation, perpendicular to the c axis, at the points indicated by the arrows of the same color in Figs. 3(d) and 3(e). The blue and red traces are those at the minima and maxima, respectively, and show that the dislocation width is ~2.5 nm. We note that while the dislocation did not change appearance prior to, during, and after the measurement, we cannot rule out the end of the dislocation being dynamic and moving on a time frame below the exposure time, blurring the features.

In addition to the dislocation stability, compared to the simulations, there are two key differences in the experiment. First, the nonzero x component of induction is not observed in the experiment at low or high fields, as shown in Fig. S4 [22]. In both cases, this may be in part because of the reduced sensitivity of the imaging technique to this particular component, as discussed above (see Fig. S2 [22]) and, potentially, because the dislocation may be dynamic (see Fig. S7, discussed later [22]). At high fields, the dislocation may additionally be modified by being pinned against a barrier. It is, however, unclear why no x component is seen at low field, but it may be related to the dense nature of the lattice in the experiment which would favor the moments remaining aligned with the ab plane. Second, the dislocation widths along the ab plane can be significantly modulated by the applied field strength, from approximately 60 nm at low field to around 2.5 nm at high field. Since these measurements are of the y component of the induction, the z component of the magnetization reversal width is very likely to be much smaller. These deviations from the simulations open the possibility to reproducibly locate and stabilize normally unstable or metastable dislocations and to modify their properties in ways not possible in uniform thickness films.

B. Hysteretic chiral soliton lattice dislocation populations

The formation and subsequent movement of dislocations is one means by which solitons may be nucleated or annihilated [15] and thus we may expect them to play a significant role in transitions to and from the F-FM and CSL phases. To investigate this, we observed the transition between these phases by Fresnel imaging [26] of a thin lamella sample of several microns in size. The results of this are depicted in Fig. 5 and show that the dislocation properties strongly depend on whether the transition is from F-FM to CSL or

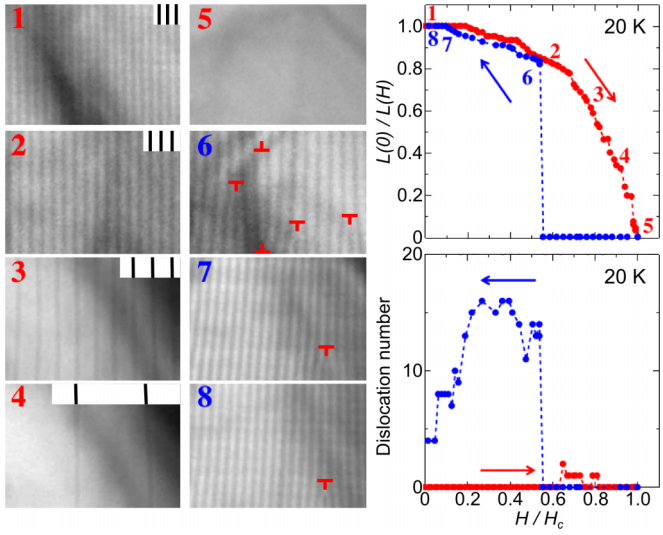

FIG. 5. Hysteretic field-dependent soliton density and dislocation population in a CSL, obtained from Fresnel imaging of a thin-film lamella at 20 K with the field, applied perpendicular the c axis and to the sample surface, swept in both the increasing (red labels) and decreasing (blue labels) directions, as indicated by the arrows in the right hand panels. 960 × 670 nm sections of the Fresnel images are shown in the left-hand panels, where dislocations are marked by rotated red "⊥" symbols, while statistics were gathered from a fixed area of 2060 × 1540 nm.

vice versa. Solitons in the Fresnel images in the left-hand panels appear at high fields as thin dark vertical lines on a variable intensity background (occurring due to bend contours in the weakly curved sample diffracting intensity away from the detector by different amounts), as shown by the black and white overlays in the left-hand column. Panels 1–5, labeled with a red font, show the transition from the CSL phase to the F-FM one as the applied field strength increases from zero to the critical field, H_c, while panels 6–8 (blue font) show the return to zero field. The results of an analysis of this and data over an area five times wider than that shown in the figure at intermediate fields to extract the field dependence of the soliton period $L(H)$ and dislocation density are shown in the upper and lower right-hand panels of Fig. 5, respectively.

The CSL to F-FM transition (red symbols in Fig. 5) is characterized at low fields by a relatively smooth, near-continuous stepped increase in soliton period as solitons are removed from the system in a stochastic process. At higher fields, there are fewer solitons and removal of a single soliton has a proportionally larger effect, resulting in increasingly large jumps in period. Importantly, very few dislocations form across the entire phase transition. This suggests that expulsion of solitons from the system is a coherent process that maintains the long-range lattice order, and that the energy barrier to annihilation is relatively low. These observations are consistent with reports of annihilation occurring due to "unzipping" of solitons as the result of the formation and rapid movement of a dislocation perpendicular to the c axis [15,29], and with our observations of dislocation movement, discussed later.

The F-FM to CSL transition (blue symbols in Fig. 5) shows markedly different behavior; the system remains in the F-FM phase until the field is reduced to around $0.55H_c$ (labeled point 6), at which field a high number of solitons appear as the phase changes from a "supercooled" F-FM phase to a CSL one with a similar periodicity to that at the same field in the opposite transition direction, but with very many dislocations. The number of dislocations remains relatively high throughout the transition to the CSL phase at a near-zero field, gradually reducing in number as the field is decreased and metastable dislocations are removed and new solitons enter the lattice.

We note that a few solitons remain at near-zero field in the decreasing branch, indicated by point 8 in Fig. 5. The applied field strength at this point was set by the residual field of the transmission electron microscope objective lens and was around 100 Oe. However, when the field polarity is swapped, equivalent to point 1 in Fig. 5, the dislocations disappear and the ideal CSL is obtained. This picture is consistent with the behavior observed in ferromagnetic resonance (FMR) experiments (discussed later) when sweeping the field applied to a sample in the F-FM state through zero.

Our direct observations via Lorentz TEM (at a lower temperature 20 K) strongly support the picture obtained based on the magnetoresistance data already reported in samples with similar dimensions [13]. In smaller volume samples, different results are obtained. When the sample is reduced in size by crystallographic chirality [13], soliton dislocations appear at the edge of the sample and move inwards, towards a step increase in thickness, as shown in Fig. S6 [22]. Because of the small volume and the stabilizing effect of the thickness step, the number of nucleation sites is reduced and more symmetric behavior with respect to the field cycle is seen in the dislocation densities. Crystal lattice grain boundaries have been shown to influence topological magnetic configurations in other chiral systems (Ref. [3] of the Supplemental Material) and may also play some role here (see [22] for further discussion).

This sample size-dependent hysteretic behavior is similar to that observed in magnetoresistance and magnetic torque measurements on micron-sized samples [12,13] and suggests there is a significant energy barrier to initial soliton nucleation. This is consistent with recent modeling efforts which predict that the transition from a supercooled F-FM to CSL phase occurs in small samples by the creation and penetration of solitons from the edge of the sample [15], and that a barrier of magnitude $(4/\pi^2 \approx 0.4)H_c$ is formed by twists of the magnetization at the surface of the sample from which they enter [30]. We note this value is similar to the one we observe in the TEM data in Fig. 5 of $0.55H_c$, and that the precise value will vary with sample-dependent demagnetization effects [30].

In all but the smallest samples, the process of solitons entering the system may occur from several edges or nucleation points, depending on the local demagnetization field [31] and, where the CSL lattices meet, metastable dislocations may form. Evidence of dislocation instability is shown in Fig. S7 [22], which demonstrates that dislocations in $CrNb_3S_6$ at a constant temperature and under a constant applied field exhibit slow dynamics, on the order of seconds, similar to observations of dislocations in the helimagnetism of FeGe [29].

C. Resonance properties of the chiral soliton lattice

In addition to dislocations exhibiting slow dynamics, one might expect them to also influence the fast magnetization dynamics of the system. However, since the volume and coherence of the dislocations will be relatively small, the direct effect will most likely be limited to modification of the resonance linewidth, as is predicted to occur in nonchiral ferromagnets with crystal defects [32]. Instead, we expect that the dominant effect of dislocations will be the indirect one, where the presence or movement of dislocations may either mediate the creation or indicate the presence of multiple CSL and F-FM regions within the sample, depending on the sweep direction, as discussed in the previous section. In addition, dislocations may also define multiple regions of dense lattices between which exist relative periodicity and phase changes in the rotation of the moment.

To probe the microwave frequency dynamics of the material in its different phases, we performed ferromagnetic resonance (FMR) measurements on a sample with a 50-μm-long chiral axis at 50 K in a custom system [14] comprising a vector network analyzer coupled to a broadband waveguide (see Fig. S8 for further details [22]). FMR data recorded while the field was swept from +0.2 to −0.2 T, after normalization and processing, is shown in Fig. 6(a). To aid interpretation of the complex spectra, the main resonance branches are highlighted in the sketch overlay shown in Fig. 6(b). In the following, we will restrict our discussion to the main features of the FMR data. A more detailed FMR study is reported elsewhere [33].

The general FMR features are similar to those reported previously from a smaller sample with with the dc field applied perpendicular to the c axis [14], with Kittel-like modes with a square root of frequency dependence [34] at high-field magnitudes ($\gtrsim$150 mT) when the sample is in the F-FM phase, and asymmetric CSL-phase resonances at lower fields. The multiple F-FM resonances are related to the existence of a size-dependent inhomogeneous demagnetization field [31]. In the larger sample used here, the CSL modes resemble a rotated sigmoid and the resonances are more complex, with the number of resonance branches varying greatly as the field is swept and the magnetization transitions between different phases.

The end of a clear single-domain F-FM phase with decreasing field occurs around +136 mT, while the transition from the CSL phase to a the F-FM one occurs at −156 mT, as indicated in the figure annotations. Due to the FMR sample being much larger than the sample used for the dislocation density measurements shown in Fig. 5, the critical F-FM fields measured in the FMR sample are relatively similar. However, they are not identical, and the discrepancy of the values is ascribed to the existence of the surface barrier in the sample, as discussed in the literature [15,30]. Only in bulk samples (0.1–1 mm along the c axis) [35] are discretization-related hysteresis effects absent.

The coexistence of CSL and F-FM regions in the F-FM to CSL transition is readily apparent from the overlapping Kittel-like and CSL-like resonances at positive fields below 136 mT. The collective resonance properties of each of these regions will be determined by the region size and on the surrounding magnetization state which, in turn, are defined in part by the dislocation distribution. The dislocations may act as pinning sites or spin-wave scatterers through distortion of the lattice, which at low fields can extend over 100 nm in range [see Fig. 4(b)]. Indeed, modeling of collective resonances in a confined CSL shows that the boundary conditions of the lattice and its soliton chain length influence the resonance frequency [36], with lower pinning fields and shorter chains having lower frequencies. We may thus tentatively ascribe the multiple low-amplitude and low-frequency FMR branches observed here to a combination of a distribution of different CSL chain lengths, CSL region sizes and boundary conditions, and F-FM regions, all defined by dislocations; in effect, the sample may be partitioned into smaller magnetic regions, each with a different low-amplitude precessional mode. As the field is reduced, the progression of dislocations through the system modifies the local boundaries of the effective volumes contributing to a given mode. In this picture, when one or more dislocations defining a region vanishes, the small-amplitude resonances from the associated volumes increase in frequency or disappear altogether while simultaneously

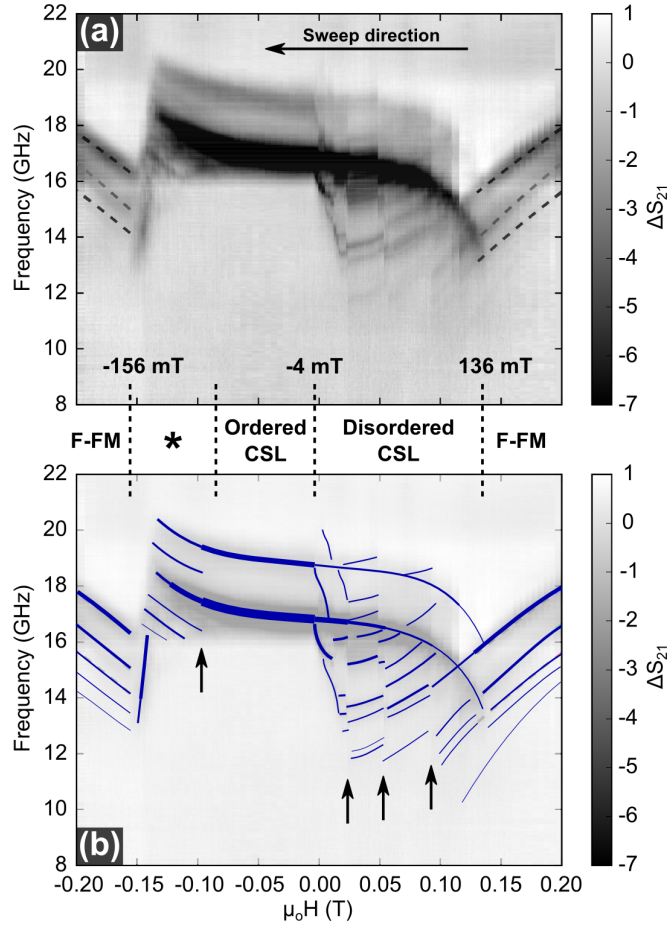

FIG. 6. Ferromagnetic resonance measurements on a specimen with a 50-μm-long chiral axis at 50 K as the dc applied field is varied from +0.2 to −0.2 T in 1 mT steps, showing how the dynamic magnetic properties are influenced by the magnetic phase. (b) A simplified sketch of (a) where the lines pick out the main resonance branches. The vertical arrows highlight examples where multiple branches jump in frequency together. The field region marked by an "*" has mixed characteristics and is discussed in the main text.

increasing the amplitude of the main CSL modes. The sharp, steplike nature of the frequency change and the high degree of synchronization (e.g., aligned jumps in frequency marked by vertical arrows in Fig. 6) is consistent with the dislocation generation and movement which, as discussed earlier, occurs very rapidly in uniform thickness samples. Only when a small negative field is reached are all dislocations finally removed from the system, consistent with the TEM data in Fig. 5, leaving it in the ordered CSL phase with a macroscopic coherence length, and only the main CSL resonance modes are observed.

Because the expulsion of solitons from an ordered CSL phase is a coherent process which maintains long-range lattice order, only modes characteristic of a single-domain CSL phase are observed until relatively large negative fields are applied and, consequently, the CSL to F-FM transition is much sharper. At fields just above the CSL to F-FM critical field there occurs a small and gradual redistribution of resonance intensity from the main CSL resonance to lower-frequency branches [marked by an "*" in Fig. 6]. While the origin of this behavior is unclear, it is interesting to note that a small number of dislocations are observed in the equivalent TEM data at this stage of reversal (see Fig. 5) and thus these may also influence the formation of CSL and F-FM regions in the CSL to F-FM transition.

Quantization effects and the macroscale coherence of the CSL phase are key properties of the $CrNb_3S_6$ system for potential application in areas of spintronics and nanomagnetism, and so it is important that further theoretical work is performed to understand in greater detail the role of disorder in these effects and also the influence of surface spins on this interesting and highly configurable magnetic system.

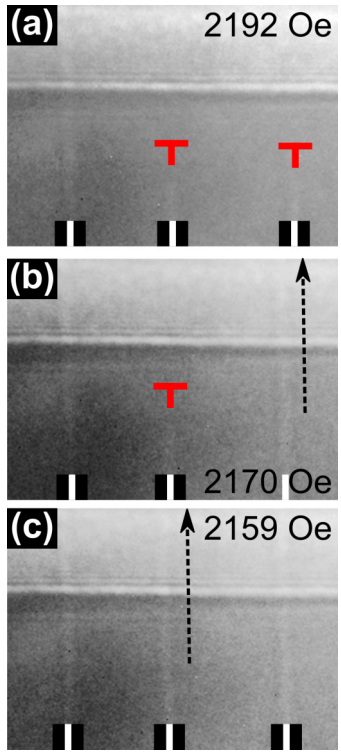

FIG. 7. Fresnel imaging of solitons running vertically in a thin lamella, showing unidirectional guided motion of soliton dislocations (rotated red "⊥" symbols) in response to a decreasing (a)–(c) applied magnetic field during the F-FM to CSL phase transition. The two different background intensities are due to thickness variations in the sample.

D. Guided motion in dislocation mediated phase transitions

Finally, evidence for field-driven dislocation movement modulating CSL growth is presented in the Fresnel images of the magnetic state at different stages of the F-FM to CSL phase transition depicted in Fig. 7. Dislocations, marked by the rotated red "⊥" symbols, move upwards following the black arrows as the field is decreased in Figs. 7(a)–7(c), enlarging the CSL area. In following the lowest-energy path, the dislocation movement allows each soliton to follow the surrounding lattice in a "guided" manner, irrespective of crystal thickness. Interestingly, this guided movement persists even in very dilute CSL phases, as shown in Fig. S9 [22]. Just as large crystal thickness steps stabilize dislocations, this field-driven guided dislocation motion may be made possible by the thickness modulation in gradually tapered samples such as that in Fig. S9 [22], further demonstrating the robust nature of solitons in $CrNb_3S_6$ and the ability to tailor their properties through changes in sample morphology. Control of the dislocation position and the size of the CSL phase in this way may be exploited in device applications such as in guiding microwave fields or in field-dependent microwave attenuators.

V. CONCLUSIONS

We have experimentally characterized the magnetization in the $CrNb_3S_6$ system at multiple length scales, from nanometer-scale resolved DPC images of chiral soliton lattice distortion at dislocations, through micron-scale Fresnel imaging of dislocation populations and the lattice parameter during magnetization reversals, to the tens of microns scale with FMR measurements of the dynamic magnetization properties. The formation and movement of soliton dislocations is found to mediate the formation of F-FM and CSL regions and this can be highly hysteretic. The dislocations strongly influence the magnetization reversal and the resulting coherence of the magnetic configuration, knowledge of which is critical to understanding and controlling the magnetization properties. Sample morphology is found to play a key role in stabilizing normally unstable or metastable dislocations and allows the magnetic properties to be controlled and modified far beyond that predicted for a uniform sample, potentially allowing the use of the tunable emergent nanochannels of field-polarized spins in device applications.

Original data files are available from the University of Glasgow Enlighten: Research Data repository [37].

ACKNOWLEDGMENTS

This work was supported by the Engineering and Physical Sciences Research Council (EPSRC) of the U.K. under Grant No. EP/M024423/1 and the JSPS Core-to-Core Program "Advanced Research Networks." We acknowledge support from the JSPS Grants-in-Aid for Scientific Research (No. 25220803, No. 17H02767, and No. 17H02923). This

work was also supported by Chirality Research Center (Crescent) in Hiroshima University. F.G. received additional support from the JSPS International Research Fellowship No. 17F17316. G.W.P. thanks William Smith for preparing the STEM lamella. Y.T. and T.K. thank Y. Fujiyoshi for the opportunity to use the seventh generation cryogenic transmission electron microscope suitable for TEM observations at low temperatures for many hours.

[1] I. E. Dzyaloshinskii, Zh. Eksp. Teor. Fiz. **46**, 1420 (1964) [J. Exp. Theor. Phys. **19**, 960 (1964)].
[2] Y. Togawa, T. Koyama, K. Takayanagi, S. Mori, Y. Kousaka, J. Akimitsu, S. Nishihara, K. Inoue, A. S. Ovchinnikov, and J. Kishine, Phys. Rev. Lett. **108**, 107202 (2012).
[3] J. Kishine and A. Ovchinnikov, in *Solid State Physics*, edited by R. E. Camley and R. L. Stamps (Elsevier, Amsterdam, 2015), Vol. 66, pp. 1–130, Chap. 1.
[4] Y. Togawa, Y. Kousaka, K. Inoue, and J. Kishine, J. Phys. Soc. Jpn. **85**, 112001 (2016).
[5] A. Fert, N. Reyren, and V. Cros, Nat. Rev. Mater. **2**, 17031 (2017).
[6] T. Moriya and T. Miyadai, Solid State Commun. **42**, 209 (1982).
[7] I. Dzyaloshinsky, J. Phys. Chem. Solids **4**, 241 (1958).
[8] T. Moriya, Phys. Rev. **120**, 91 (1960).
[9] T. Miyadai, K. Kikuchi, H. Kondo, S. Sakka, M. Arai, and Y. Ishikawa, J. Phys. Soc. Jpn. **52**, 1394 (1983).
[10] M. Shinozaki, S. Hoshino, Y. Masaki, J. Kishine, and Y. Kato, J. Phys. Soc. Jpn. **85**, 074710 (2016).
[11] V. Laliena, J. Campo, and Y. Kousaka, Phys. Rev. B **94**, 094439 (2016).
[12] J.-I. Yonemura, Y. Shimamoto, T. Kida, D. Yoshizawa, Y. Kousaka, S. Nishihara, F. J. T. Goncalves, J. Akimitsu, K. Inoue, M. Hagiwara, and Y. Togawa, Phys. Rev. B **96**, 184423 (2017).
[13] Y. Togawa, T. Koyama, Y. Nishimori, Y. Matsumoto, S. McVitie, D. McGrouther, R. L. Stamps, Y. Kousaka, J. Akimitsu, S. Nishihara, K. Inoue, I. G. Bostrem, V. E. Sinitsyn, A. S. Ovchinnikov, and J. Kishine, Phys. Rev. B **92**, 220412(R) (2015).
[14] F. J. T. Goncalves, T. Sogo, Y. Shimamoto, Y. Kousaka, J. Akimitsu, S. Nishihara, K. Inoue, D. Yoshizawa, M. Hagiwara, M. Mito, R. L. Stamps, I. G. Bostrem, V. E. Sinitsyn, A. S. Ovchinnikov, J. Kishine, and Y. Togawa, Phys. Rev. B **95**, 104415 (2017).
[15] M. Mito, H. Ohsumi, K. Tsuruta, Y. Kotani, T. Nakamura, Y. Togawa, M. Shinozaki, Y. Kato, J.-i. Kishine, J.-i. Ohe, Y. Kousaka, J. Akimitsu, and K. Inoue, Phys. Rev. B **97**, 024408 (2018).
[16] S. McVitie, D. McGrouther, S. McFadzean, D. MacLaren, K. O'Shea, and M. Benitez, Ultramicroscopy **152**, 57 (2015).
[17] J. N. Chapman, I. R. McFadyen, and S. McVitie, IEEE Trans. Magn. **26**, 1506 (1990).
[18] T. Malis, S. C. Cheng, and R. F. Egerton, J. Electron Microsc. Tech. **8**, 193 (1988).
[19] FPD: Fast pixelated detector data storage, analysis and visualization, https://gitlab.com/fpdpy/fpd (accessed May 23, 2019).
[20] F. de la Peña, V. T. Fauske, P. Burdet, E. Prestat, P. Jokubauskas, M. Nord, T. Ostasevicius, K. E. MacArthur, M. Sarahan, D. N. Johnstone, J. Taillon, A. Eljarrat, V. Migunov, J. Caron, T. Furnival, S. Mazzucco, T. Aarholt, M. Walls, T. Slater, F. Winkler *et al.*, hyperspy/hyperspy v1.4.1 (2018), 10.5281/zenodo.1469364.
[21] F. Yoshinori, Protein Sci. **20**, 806 (2011); Proc. Jpn. Acad., Ser. B **91**, 447 (2015).
[22] See Supplemental Material at http://link.aps.org/supplemental/10.1103/PhysRevB.99.224429 for examples of simulated DPC images, measured dislocation induction components, sample overview images, reversal properties in a confined geometry, examples of dislocation instability, details of the FMR setup, and evidence of dislocation guided motion in dilute CSL phases.
[23] M. Beleggia, M. A. Schofield, Y. Zhu, M. Malac, Z. Liu, and M. Freeman, Appl. Phys. Lett. **83**, 1435 (2003).
[24] S. McVitie, G. S. White, J. Scott, P. Warin, and J. N. Chapman, J. Appl. Phys. **90**, 5220 (2001).
[25] J.-i. Kishine and A. S. Ovchinnikov, Phys. Rev. B **79**, 220405(R) (2009).
[26] J. Chapman and M. Scheinfein, J. Magn. Magn. Mater. **200**, 729 (1999).
[27] J. Kishine, K. Inoue, and Y. Yoshida, Prog. Theor. Phys. Suppl. **159**, 82 (2005).
[28] R. Abbaschian, L. Abbaschian, and R. E. Reed-Hill, *Physical Metallurgy Principles* (Cengage Learning, Boston, 2008).
[29] A. Dussaux, P. Schoenherr, K. Koumpouras, J. Chico, K. Chang, L. Lorenzelli, N. Kanazawa, Y. Tokura, M. Garst, A. Bergman, C. L. Degen, and D. Meier, Nat. Commun. **7**, 12430 (2016).
[30] M. Shinozaki, Y. Masaki, R. Aoki, Y. Togawa, and Y. Kato, Phys. Rev. B **97**, 214413 (2018).
[31] F. J. T. Goncalves, T. Sogo, Y. Shimamoto, I. Proskurin, V. E. Sinitsyn, Y. Kousaka, I. G. Bostrem, J. Kishine, A. S. Ovchinnikov, and Y. Togawa, Phys. Rev. B **98**, 144407 (2018).
[32] V. G. Bar'yakhtar, M. A. Savchenco, and V. V. Tarasenko, Zh. Eksp. Teor. Fiz. **54**, 1603 (1968) [J. Exp. Theor. Phys. **27**, 858 (1968)].
[33] F. J. T. Goncalves, Y. Shimamoto, T. Sogo, G. W. Paterson, Y. Kousaka, and Y. Togawa, arXiv:1903.10129.
[34] C. Kittel, Phys. Rev. **73**, 155 (1948).
[35] Y. Togawa, Y. Kousaka, S. Nishihara, K. Inoue, J. Akimitsu, A. S. Ovchinnikov, and J. Kishine, Phys. Rev. Lett. **111**, 197204 (2013).
[36] J.-i. Kishine, I. Proskurin, I. G. Bostrem, A. S. Ovchinnikov, and V. E. Sinitsyn, Phys. Rev. B **93**, 054403 (2016).
[37] G. W. Paterson, T. Koyama, M. Shinozaki, Y. Masaki, F. J. T. Goncalves, Y. Shimamoto, T. Sogo, M. Nord, Y. Kousaka, Y. Kato, S. McVitie, and Y. Togawa, Research data for "Order and Disorder in the Magnetisation of the Chiral Crystal $CrNb_3S_6$," University of Glasgow, http://dx.doi.org/10.5525/gla.researchdata.829 (2019).